

# Low variability runoff inhibits coupling of climate, tectonics, and topography in the Greater Caucasus

## Expanded Methods and Figures

Adam M. Forte<sup>1</sup>, Joel S. Leonard<sup>2</sup>, Matthew W. Rossi<sup>3</sup>, Kelin X. Whipple<sup>2</sup>, Arjun M. Heimsath<sup>2</sup>, Lasha Sukhsvili<sup>4</sup>, Tea Godoladze<sup>4</sup>, and Fakhraddin Kadirov<sup>5</sup>

<sup>1</sup>Department of Geology & Geophysics, Louisiana State University, Baton Rouge, LA, USA

<sup>2</sup>School of Earth and Space Exploration, Arizona State University, Tempe, AZ, USA

<sup>3</sup>Earth Lab, Cooperative Institute for Research in Environmental Sciences (CIRES), University of Colorado, Boulder, CO, USA

<sup>4</sup>Institute of Earth Sciences and National Seismic Monitoring Center, Ilia State University, Tbilisi, Georgia

<sup>5</sup>Institute of Geology and Geophysics of Azerbaijan National Academy of Sciences, Baku, Azerbaijan

## Contents

<b>1 Data Availability</b>	<b>2</b>
<b>2 Expanded Methods</b>	<b>2</b>
2.1 $^{10}\text{Be}$ Sample Site Selection . . . . .	2
2.2 $^{10}\text{Be}$ Sample Processing . . . . .	2
2.3 Erosion Rate Calculation . . . . .	3
2.4 Topographic, Tectonic, and Climatic Analysis . . . . .	3
2.4.1 Basin Averaged Analyses . . . . .	3
2.4.2 Convergence Gradient . . . . .	3
2.5 Evaluating Influence of Lithology on Topography, Quartz Sourcing, and Erosion Rates . . . . .	4
2.6 Fitting a Stream Power Incision Model Based Relationship Between $k_{\text{sn}}$ and Erosion Rate . . . . .	4
2.7 Discharge, Runoff, and Variability in the Caucasus in Gauged Basins . . . . .	5
2.8 Estimating Hydroclimatic Parameters in Ungauged Basins . . . . .	6
2.9 Application of the Stochastic Threshold Incision Model . . . . .	7
2.9.1 Parameterization and Application of the STIM Relationship in the Caucasus . . . . .	7
<b>3 Supplemental Table Captions</b>	<b>9</b>
3.1 Table S1 . . . . .	9
3.2 Table S2 . . . . .	9
3.3 Table S3 . . . . .	9
<b>4 Supplemental Figures and Captions</b>	<b>10</b>

## List of Figures

S1 GPS velocities . . . . .	10
S2 Flow component separation example . . . . .	11
S3 Rainfall and Runoff Time Series . . . . .	11
S4 Topography, gradient, erosion rate, and concavity . . . . .	12
S5 $\chi$ -Z plots of sampled basins . . . . .	12
S6 Quartz sourcing and erosion rates . . . . .	13

S7	Power law fit of data . . . . .	14
S8	Distribution fit methodology . . . . .	15
S9	Comparison of distribution fits . . . . .	15
S10	Channel width data from erosion rate basins . . . . .	16
S11	Cluster number selection . . . . .	16
S12	Variation of optimized $k_e$ , $\tau_c$ and lithology . . . . .	17
S13	Spatial variation in erosion rates . . . . .	18
S14	Topography correlations . . . . .	19
S15	Topography and lithology comparisons for all basins . . . . .	20
S16	Comparison of components and discharge distribution . . . . .	21

## 1 Data Availability

The majority of the relevant data for the sample locations and associated data (e.g. gauged watersheds) are provided as tables included in the data repository. To aid in reproducibility and ease of usage, we also provide these data as text files in a GitHub repository. In this repository we also provide selected analysis scripts (these are highlighted in the supplemental methods document that follows), shapefiles, and rasters necessary to reproduce the analyses we present, along with a detailed description and figures related to the compiled lithology of each catchment. A complete list of the contents of the repository can be found in the ReadMe file in the repository.

## 2 Expanded Methods

### 2.1 $^{10}\text{Be}$ Sample Site Selection

Sample locations were pre-selected based on several criteria. We targeted basins with drainage areas between 5 - 100 km<sup>2</sup> and that did not include major knickpoints within their profiles or major variations in mean local relief (2500 m window) or normalized channel steepness ( $k_{sn}$ ). The lower bound on drainage area was to avoid sampling extremely small catchments whose erosion rates can be significantly biased by landsliding events [Yanites et al., 2009, Niemi et al., 2005] and the upper bound was designed to avoid averaging over large spatial areas where erosion rates may vary due to tectonic heterogeneity (e.g. basins spanning across major structures, etc). We additionally avoided sampling catchments which included areas that were currently glaciated or had been glaciated during the last glacial maximum [Gobejishvili et al., 2011]. We attempted to select sample basins with minimal lithologic heterogeneity, but were limited by geopolitical constraints on possible sample locations. We also made an effort to sample across a wide range of mean annual rainfall rates and basin mean normalized channel steepness.

In the field, sample sites were evaluated for potential local landslide activity and human modification and when possible, we sampled river sediments upstream of settlements. Additionally, we attempted to sample tributaries at least 500 meters in elevation above their confluences with major trunk streams to avoid sampling reworked sediment that could have been deposited as a result of landslide dams on major streams. Sediment samples were preferentially taken from the active channels or bar deposits without vegetation. In total, we collected 76 samples (Table S2).

### 2.2 $^{10}\text{Be}$ Sample Processing

Of the 76 total samples, based on their spatial distribution, coverage of parameter space as defined by normalized channel steepness and mean annual precipitation rates, and additional field or topographic observations, we selected 47 samples to process for  $^{10}\text{Be}$ . All samples were processed in the Surface Processes WOMBAT Laboratory in the School of Earth and Space Exploration at Arizona State University. Samples were wet sieved to 250-1000  $\mu\text{m}$  and then air dried. All samples were cleaned in a 1:1 solution of HCl and HNO<sub>3</sub> at room temperature for 24 hours. Because of the abundance of quartz rich lithic clasts within the samples, initial attempts at standard HF and HNO<sub>3</sub> leaches to clean and concentrate quartz [e.g. Kohl and Nishizumi, 1992] were unsuccessful, and thus we needed to implement the much more labor and time intensive Hot Phosphoric Acid (HPA) technique [Mifsud et al., 2013]. Through trial and error, we modified the original HPA technique to a three step process where in small (80g) aliquots of the sample were first boiled in a 50% solution of NaOH for 10-20 minutes, allowed to cool, and then washed thoroughly to decant off the fine grained residue. Then the remainder of the sample was slowly heated to 220°C in 80% orthophosphoric acid (H<sub>3</sub>PO<sub>4</sub>) to form pyrophosphoric acid (H<sub>4</sub>P<sub>2</sub>O<sub>7</sub>) and then leached in this solution for 30-60 minutes. Finally, after cooling, the samples were washed thoroughly and boiled in another 50% solution of NaOH for 15-30 minutes

and then, after cooling, washed and dried. The modified HPA technique was successful in removing the majority of feldspars and/or disaggregating lithic components present within the samples.

After the HPA, minerals denser than  $2.85 \frac{g}{cm^3}$  were removed via lithium polytungstate (LST) density separation. To purify quartz in the remaining material, it was leached in 1-5% HF and  $HNO_3$  solutions on heated rollers for at least 12 hours. Quartz yields for the majority of samples were very low (<5%), despite large masses (>1500g) of processed sample (Table S2). Of the original 47 samples, only 35 samples had sufficient quartz to proceed. Remaining quartz was spiked with either commercial or a low-background  $^{9}Be$  carrier and digestions for purified quartz in HF and  $HNO_3$  lasted for 7-10 days. Standard blank samples were processed along with each distinct batch of samples. We removed cations and anions using standard liquid chromatography techniques [Ditchburn and Whitehead, 1994]. Oxidized beryllium was mixed with a niobium matrix and loaded into cathodes for analysis at PRIME Lab, Purdue University. Beryllium isotope ratios for samples and blanks were referenced to isotope ratios defined in the 07KNSTD (Table S3). One sample (92715-2), which had been particularly problematic during the liquid chromatography steps, came back with 0 measured  $^{10}Be$ , but spatially was surrounded by samples with very low erosion rates, thus we do not interpret this as a high erosion rate sample, but rather some sort of chemical processing error, and as such we exclude this from Table S3 and other subsequent results.

## 2.3 Erosion Rate Calculation

To calculate the catchment averaged erosion rates, we use the approach of Portenga and Bierman [2011], wherein for each basin we identify a single effective elevation, latitude, and longitude to approximate a suitable production rate of  $^{10}Be$  for the entire basin. To accomplish this, we use topography for each basin from the Shuttle Radar Topography Mission (SRTM) 30-m digital elevation model and calculate a scaled  $^{10}Be$  production rate based on the elevation and latitude of each pixel, using the production rate from spallation reactions using the scheme by Stone [2000]. From this, we calculate the mean production rate and then find the elevation and latitude (i.e. the effective latitude and elevation) within the basin that corresponds to this production rate. We use this effective latitude and elevation, along with the longitude of the centroid of the sampled basin and the calculated  $^{10}Be$  concentrations in the online exposure age calculator formerly known as the CRONUS-Earth online exposure age calculator [Balco et al., 2008], v3.0 (accessed August 2019). Parameters used for erosion rate calculations are provided in Table S2. We assume no topographic shielding as this effect is usually small and has generally been shown to be unnecessary in steep landscapes [DiBiase, 2018]. We report erosion rates from all three schemes as reported by the calculator in Table S3, but elsewhere only use the time independent 'St' estimate using the scheme of Stone [2000].

## 2.4 Topographic, Tectonic, and Climatic Analysis

The analysis of topography, convergence rate, and basic climate variables largely follow prior efforts presented in Forte et al. [2014] and Forte et al. [2016]. We briefly review relevant methods in the following sections, focusing primarily on any updates from the original methodologies.

### 2.4.1 Basin Averaged Analyses

We use the Shuttle Radar Topography Mission (SRTM) 30 meter digital elevation model and a combination of TopoToolbox [Schwanghart and Scherler, 2014] and the Topographic-Analysis-Kit [TAK; Forte and Whipple, 2019] to calculate basin averaged statistics. For calculation of normalized channel steepness ( $k_{sn}$ ), we use a reference concavity of 0.50, a smoothing length of 1000 m, the 'ksn\_quick' method within TAK and for hillslope gradients we use the 'arcslope' method within the base TopoToolbox gradient8 function. We report a variety of basic topographic statistics and metrics, including elevation,  $k_{sn}$  (across a range of concavity values), gradient, and the best fit concavity and  $\chi R^2$  for each basin (Table S3). The  $\chi R^2$  statistic describes the extent to which the relationship between  $\chi$  and elevation is linear. A steady state basin with no knickpoints should have a linear  $\chi$  and elevation relationship and thus a  $\chi R^2$  value close to 1.  $\chi R^2$  values for basins generally are a better indicator of potential disequilibrium than either the standard deviation or standard error of the mean of  $k_{sn}$  as these metrics more reflect noise in the underlying DEM. All but two of the reported basins (16AF01 and 90216-1) have  $\chi R^2$  values  $> 0.9$ , and  $\chi R^2$  of trunk stream values  $>$  than 0.97, indicating the majority of these basins lack major knickpoints (Figure S5). The knickpoints in 16AF01 and 90216-1 are not extreme and neither of these basins represent outliers in  $k_{sn}$  or erosion rate space, thus we do not think that their inclusion in the analysis is inappropriate, however we evaluate their exclusion from the dataset in a later section.

### 2.4.2 Convergence Gradient

We follow the methodology discussed in Forte et al. [2014] in calculating along-strike gradients in convergence within the Greater Caucasus. The calculation uses the same original data used by Forte et al. [2014], but also includes additional stations

and updated observations at some stations from Sokhadze et al. [2018]. As in Forte et al. [2014], we classified GSP stations as either being in the Lesser or Greater Caucasus, largely using the block boundaries defined by Reilinger et al. [2006] (Figure ??). We then use TAK [Forte and Whipple, 2019] to project the locations of these selected stations onto the swath along the crest of the Greater Caucasus so that they have a common reference frame with the erosion rate basins. For stations defined as 'Lesser Caucasus' or 'Greater Caucasus', we calculate a smoothed N25°E velocity by taking the average within a moving 50 km window which is interpolated over the along-strike length of main the swath (dashed lines in the bottom of Figure S1). We calculate similar moving averages for the extremes of both datasets using the uncertainty on the GPS velocities (shaded regions in the bottom of Figure S1). We then use similar assumptions as Forte et al. [2014] and difference the Lesser Caucasus and Greater Caucasus velocities. This difference is interpreted as an approximation of the amount of convergence along the southern margin of the Greater Caucasus, with the remaining velocity of the Greater Caucasus accommodated as convergence within the range or along its northern flank.

## 2.5 Evaluating Influence of Lithology on Topography, Quartz Sourcing, and Erosion Rates

To assess the potential role that lithology plays in influencing our results, either in terms of variable sourcing of quartz or topographic statistics, for each sampled catchment we digitized available geologic maps and compiled lithologic information. These complied geologic maps and details of the sources from which they were compiled are available in the GitHub repository. Using these digitized lithologic classifications, we then used the functionality within TAK [Forte and Whipple, 2019] to calculate the percent of each catchment occupied by specific lithologies, which are reported in Table S3. For each catchment, we produced explorative plots to assess whether the distribution of lithologies had meaningful contributions to the topographic metrics (i.e.  $k_{sn}$  and slope gradient). While many catchments exhibit at least some degree of correlation between values of  $k_{sn}$  or gradient and lithology, none of these patterns appear consistent, i.e. no particular lithology appears to always be steeper or shallower across catchments (Figure S15). The only lithologies that appear to have consistent  $k_{sn}$  or gradients, or values of either that differ substantially from the statistics of the population as a whole, are those which represent very small portions of the area and as such, we do not think this is diagnostic of the representation of a lithologic influence on topography, but rather a reflection of the topography of the specific catchments which include these lithologies.

More critically, given the documented extremely low quartz yields from all samples (e.g. Table S3), we also tested the sensitivity of the calculated erosion rates to variable quartz sourcing based on lithologic heterogeneity. We first recalculated appropriate latitudes and elevations for the production rate calculations again using the method of Portenga and Bierman [2011], but after filtering out portions of any catchments with dominantly carbonate lithologies, specifically those classified as 'limestone', 'limestone and marl', and 'marl'. We did not filter out 'limestone and minor clastics' and 'limestone and sandstone' as we assumed these units may still contribute sufficient quartz from their clastic constituents. We then used these updated elevation and latitude values in the online erosion rate calculator (Table S3) and paired this with mean basin  $k_{sn}$  values calculated excluding the same portions of each watershed. The calculated erosion rates, mean basin  $k_{sn}$  values, mean basin gradient, and pattern between erosion rates and either topographic metric was not appreciably different after filtering out these dominant carbonate lithologies (Figure S6)

Given the uncertainty in individual unit descriptions (and unknown quartz concentrations within the units), we additionally tested two end member schemes for calculation of production and erosion rates along with topography. For these schemes, we assumed that either all of the quartz was sourced from the bottom or top 50% of the catchment and calculated appropriate elevations and latitudes for use in the online calculator and topographic metrics for the respective portions of the catchments. Results from the erosion rate calculations are reported in Table S3. As with the lithological filtering, this experiment did not appreciably change the nature of the relationship between topography and erosion rate (e.g. Figure S6), thus generally we do not consider variable quartz sourcing as a source of uncertainty in the erosion rates and our subsequent conclusions.

## 2.6 Fitting a Stream Power Incision Model Based Relationship Between $k_{sn}$ and Erosion Rate

To fit a stream power incision model (SPIM) based power law relationship between  $k_{sn}$  and erosion rate, we fit the available data using a bootstrap routine, which we describe below. We also fit the data using a monte-carlo scheme similar to Adams et al. [2020], but it produced estimates of the parameters within the uncertainty bounds of the bootstrap fit, so we do not discuss present results from these.

For the bootstrap approach, we use bootstrap sampling, i.e. random sampling of a  $N$  member dataset with replacement to produce a bootstrap sample also with  $N$  members, but that may have multiple repeated entries. Each bootstrap sample draws from a set of  $k_{sn}$  - erosion rate pairs with their respective uncertainties, i.e. the relationships between  $k_{sn}$  and erosion rate for

particular samples are preserved in the bootstrap sampling process. An orthogonal distance regression fit (considering uncertainty) is performed on each bootstrap sample and this procedure is repeated an arbitrarily large number of times. Ultimately we are interested in the population of fit parameters, i.e. coefficients and exponents of the power law, and we can choose the most appropriate coefficient and exponent pair by finding the medians of these fit parameter populations. This bootstrap technique is explicitly designed to test the importance of outliers.

For each individual fit, we use the orthogonal distance regression (ODR) algorithm as implemented in SciPy and the  $k_{sn}$ -E relationship,

$$E = K(k_{sn})^n \quad (\text{S1})$$

as a log-transformed version such that it is a linear fit using,

$$\log10(E) = n * \log10(k_{sn}) + \log10(K) \quad (\text{S2})$$

We perform 1e6 individual fits and then aggregate the population of fit parameters, i.e. values of  $K$  and  $n$ . We exclude data from sample 91416-1 for all fits because the uncertainty value for erosion rate is greater than the measured rate. We also perform a second set of fits where we exclude the two highest erosion rate basins (samples 90416-1 and 90216-2) and the two basins with lower  $\chi R^2$  values (16AF01 and 90216-1, Figure S5) to estimate a more conservative set of parameters (Figure S7). We emphasize however that there is no specific reason to exclude the two high erosion rate samples, i.e. other than the erosion rate, there is nothing anomalous about these basins that cause us to question the validity of these rates.

For each population of fits, we use the median value (see bottom panel of Figure S7) of  $n$  and  $K$  to define the main curve. The shaded area is defined by the 25th and 75th percentile of the  $n$  and  $K$  values, specifically pairing the 25th percentile  $n$  with the 75th percentile  $K$  and vice versa. We use the median and quartile range because the bootstrap fit parameter distributions are skewed and thus the median and quartile range are less biased measures of the central tendency than the mean and standard deviation. Removing the two highest erosion rates and the two basins with some degree of disequilibrium does decrease the best bootstrap fit  $n$  value from 3.46 to 3.07 (primarily driven by the removal of the two high erosion rate basins), but (1) this lower  $n$  still implies a very nonlinear  $k_{sn}$  - erosion rate and thus does not appreciably change the result and (2) this lower median  $n$  is within the uncertainty bounds on the estimation of  $n$  from the fits that include these high erosion rate basins.

## 2.7 Discharge, Runoff, and Variability in the Caucasus in Gauged Basins

To characterize the details of runoff within the Caucasus region, we start with an analysis of gauged basins in the Caucasus region. Forte et al. [2016] presented such an analysis of available daily discharge data from gauged basins within the Caucasus region provided by the Global Runoff Data Centre (GRDC). Here, we use the same underlying dataset as Forte et al. [2016], but subset it to remove potentially problematic basins from the dataset which may have anomalous discharges or variability. Specifically, using publicly available satellite imagery, we manually inspected the course of rivers within the GRDC basins and removed from the dataset any basins which had visible dams.

**Discharge to Runoff:** To convert from discharge to runoff, we assume a simple relationship between drainage area and discharge,

$$Q = RA^c \quad (\text{S3})$$

where  $R$  is runoff,  $Q$  is discharge, and  $A$  is drainage area. We follow DiBiase and Whipple [2011] and assume  $c = 1$ , i.e. a linear relationship. This linear approximation appears valid, i.e. after accounting for spatial variation in rainfall rates, there is a quasi-linear relationship between discharge and drainage area (Figure 2). Results from this analysis are reported in Table S1.

**Distributions of Discharge:** It is necessary to estimate the probability distribution function appropriate for observed discharge records to eventually incorporate into the stochastic threshold incision model. A number of prior efforts [e.g., Lague et al., 2005] use a one parameter version of the inverse-gamma distribution to characterize the probability distribution function (*pdf*),

$$pdf(Q^*; k) = \frac{k^{k+1}}{\Gamma(k+1)} \exp\left(-\frac{k}{Q^*}\right) Q^{*-2-k} \quad (\text{S4})$$

where  $k$  is the shape parameter, the scale parameter is set to  $k + 1$ ,  $\Gamma$  is the gamma function, and  $Q^*$  is normalized discharge. Ultimately, the discharge data within the Caucasus was not well explained with an inverse-gamma distribution, so we instead follow Rossi et al. [2016] and use a 2 parameter Weibull distribution, where the pdf is,

$$pdf(Q^*; X_0, c) = \frac{c}{X_0} \left( \frac{Q^*}{X_0} \right)^{c-1} exp^{-1(Q^*/X_0)^c} \quad (S5)$$

where  $c$  is a shape parameter and  $X_0$  is a scale parameter. We fit individual discharge records using the Weibull distribution in two different ways. A simple fit of the whole distribution via the SciPy Weibull fit function using the method of moments (which performed better than the default maximum likelihood estimation) and a more complicated fitting procedure that fit the tail of the distribution but also attempted to minimize the misfit between the observed  $\bar{R}$  and that implied by the fit distribution. In detail, we adapt the procedure from Wilson and Toumi [2005] and used by Rossi et al. [2016] to fit the tail of a Weibull distribution above a given threshold. In this procedure, we test a range of thresholds between 0.01% and 60%, extract all observations above the threshold, linearize the selected portion of the tail via a natural log transform, and then fit a linear regression to this tail which allows us to estimate both  $c$  and  $X_0$ . We redo this over the full range of tested thresholds (Figure S8), generating a set of  $c$  and  $X_0$ . For each candidate distribution, we also calculate the implied mean runoff (i.e., the mean of the distribution in normalized discharge space multiplied by the mean runoff for the basin). To find a fit that honors the tail and the mean, we construct an minimize an objective function,

$$f = 1.5 * \frac{MSS}{max(MSS)} + \frac{|\Delta(\bar{R})|}{max(|\Delta(\bar{R})|)} \quad (S6)$$

where  $MSS$  is the mean squared error on the linear fit of the natural log linearized tail and  $\Delta\bar{R}$  is the difference between the observed and implied mean runoff. The 1.5 weighting on the mean runoff was found through trial and error. The normalization by the max values is necessary as the magnitude of  $MSS$  is quite small compared to the magnitude of  $\Delta\bar{R}$ , so without the normalization, the minimum of the objective function is heavily biased by  $\Delta\bar{R}$ . While the whole distribution fits via the method of moments more faithfully reproduce the observed mean of the runoff distributions, our composite fit does a better job honoring both the shape of the tail but also the magnitude of rarer events, which is especially important given the ultimate purpose of using these distributions in STIM where only portions of the distribution above a critical discharge or runoff are considered (Figure S9). We provide the function for fitting the distributions in the GitHub repository as *discharge\_fit.py*.

We provide a shapefile of the GRDC basins with relevant summary values in the attribute table in the GitHub repository.

## 2.8 Estimating Hydroclimatic Parameters in Ungauged Basins

**Mean Runoff** To estimate mean daily runoff in the ungauged  $^{10}\text{Be}$  sample basins, we use a spatially continuous rainfall dataset (TRMM 3B42) to estimate runoff in ungauged basins. We calculate mean daily rainfall from TRMM in each gauged basin and compare this to mean runoff then fit a power law relationship with a y-intercept through this data. We then use this relationship to predict mean runoff in the ungauged basins based on their mean rainfall from TRMM. It is worth noting that generally, gauged basins with mean runoffs below 3 mm/day have mean basin rainfall rates that are greater than their runoffs, i.e. the runoff ratio is below 1. However, consistently for basins above 3 mm/day of gauged runoff, the mean runoff exceeds the mean basin rainfall, i.e. the runoff ratio is greater than 1. Consequently, the result of power law fit between a mean rainfall rate of 4 mm/day or greater implies a runoff ratio  $>1$ . We expect that these runoff ratios  $>1$  result from an underestimation of the precipitation within the TRMM 3B42 data. TRMM 3B42 data is specifically known to underestimate precipitation that falls as snow at high elevations [e.g. Wulf et al., 2016]. We provide the function for fitting the rainfall and runoff data and estimating the runoff in ungauged basins in the GitHub repository as *estimate\_runoff.py*.

**Runoff Variability and Cluster Analysis** : Ideally, we would like to map estimations of the shape and scale parameters from the gauged runoff distributions to our ungauged basins to apply them in STIM. While there are some relationships between quantities measurable in the ungauged basins and aspects of the runoff distributions (e.g., maximum catchment elevation and the scale parameter as seen in Figure 5C), there is sufficient scatter in the relationships and a somewhat unclear basis on which to extrapolate shape and scale parameters that this did not seem a prudent direction. Instead, we divided the population of gauged basins into smaller, like groups and attempted to assess which ungauged erosion rate basins would be best characterized by the runoff distributions from these populations. We determined these populations via a k-means cluster analysis. We used  $c$  and  $\bar{R}$  as the two parameters on which to base the cluster analysis. The data was scaled prior to cluster analysis using the 'StandardScaler' in scikit-learn such that the mean of each variable is 0 and the standard deviation is 1. We tested cluster values of 1-14 and found that 4 clusters was the ideal based on a 'elbow plot' (Figure S11), though the exact choice of elbow is slightly ambiguous.

To assign individual, ungauged erosion rate basins to clusters, we use their estimated mean runoff, the elevation range of the catchments, and the geographic location of the basins with respect to the locations of gauged basins (Figure 5). While there is a clear break in  $\bar{R}$  in both gauged basins and estimated values in ungauged basins, the elevation and geography bounds are somewhat ambiguous, especially between cluster 2 and 3. For this case, we exploited the fact that one of our erosion rate basins lies inside a much larger gauged basin so we tuned the maximum elevation boundary between cluster 2 and 3 until this basin was classified the same as its parent gauged basin.

## 2.9 Application of the Stochastic Threshold Incision Model

### 2.9.1 Parameterization and Application of the STIM Relationship in the Caucasus

To apply the stochastic threshold incision model (STIM) to our data, we numerically solve for mean erosion rate  $\bar{I}$  using the a modified version of STIM presented by DiBiase and Whipple [2011]:

$$\bar{I} = \int_{Q_c^*(k_s)}^{Q_m^*} I(Q^*, k_s) pdf_{\bar{Q}_k}(Q^*) dQ^* \quad (S7)$$

where  $\bar{Q}$  is mean discharge,  $Q^*$  is normalized discharged such that  $Q^* = Q/\bar{Q}$ ,  $Q_c^*$  is the minimum discharge that will overcome  $\tau_c$  and  $Q_m^*$  is the maximum discharge observed within the considered time frame. In Equation S7, the instantaneous incision rate  $I$  is given by,

$$I = K\bar{Q}^m Q^{*\gamma} S^n - \Psi_c \quad (S8)$$

where  $K$  is erosional efficiency,  $S$  is channel slope,  $\Psi_c$  is a threshold term, and  $m$ ,  $n$ , and  $\gamma$  are empirical constants. In Equation S7, we consider the probability distribution of discharge  $pdf_{\bar{Q}_k}$  to follow a Weibull distribution (eq. S5). For a full derivation of the STIM equations and a complete discussion of their terms, we refer readers to Lague et al. [2005] or DiBiase and Whipple [2011]. Our implementation of the STIM relationships are provided in the GitHub repository as *stochastic\_threshold.py*.

From the prior results, for each erosion rate basin, we have estimates of the mean runoff and some estimation of the shape and scale parameter for the clusters to which those basins belong, but to explore the extent to which STIM relationship, considering these runoffs and variabilities, explains the observed patterns between  $^{10}\text{Be}$  erosion rates and  $k_{sn}$ , we must assign, or estimate, values of various parameters within STIM. We list the values used and their associated units below:

Parameter	Value	Units
$k_e$	Variable	$m^{2.5} s^2 kg^{-1.5}$
$R$	Variable	$m^1 s^{-1}$
$k$	Variable	Dimensionless
$\tau_c$	45	Pa
$k_w$	15	$m^{-0.5} s^{0.5}$
$k_t$	1000	$m^{-7/3} s^{-4/3} kg$
$\omega_a$	0.5	Dimensionless
$\omega_s$	0.25	Dimensionless
$a$	3/2	Dimensionless
$\alpha$	2/3	Dimensionless
$\beta$	2/3	Dimensionless

We assume a Darcy-Weisbach friction relation and set  $\alpha = \beta = 2/3$ , follow Tucker [2004] and set  $k_t = 1000$ , such that  $k_t = \rho_w g^{2/3} C_f^{1/3}$  where  $C_f = 0.08313$ , and we set  $a = 3/2$ , which assumes unit stream power. We do not have direct field observations with regards to channel width or cross sectional form, so for  $\omega_s$  we use a value of 0.25 consistent with a concave channel cross section and between the expected range of 0 to 0.5 [Lague et al., 2005]. With  $\omega_s = 0.25$ , we set  $\omega_a = 0.50$  so that the ratio of  $m/n$ , i.e. the concavity, equals 0.5 to be consistent with the reference concavity we use to calculate  $k_{sn}$ .

For  $k_w$ , which is the coefficient on the power law relationship between channel width,  $w$ , at a given discharge  $Q$ ,

$$w = k_w Q^{\omega_a} \quad (S9)$$

we use a value of 15, which is the same value used by DiBiase and Whipple [2011]. To explore whether this choice of  $k_w$  is appropriate, it is necessary to compare the predictions for channel width implied by this value, along with the value of  $\omega_a$ , to

field measurements of width. In the absence of such field measurements, we use the 'ChanGeom' tool [Fisher et al., 2013], which can be used to measure channel widths on high resolution satellite imagery. Careful measurements using this tool have been shown to be similar to field measured widths in both the Himalaya and Taiwan [e.g. Fisher et al., 2013, Yanites et al., 2018]. Specifically, we use freely available imagery in Google Earth to map channel widths and the methodology of Yanites et al. [2018] in which we map the extent of largely vegetation free, gravel areas surrounding channels, with the assumption being that this represents areas which experience flows often enough to suppress the establishment of vegetation. Where clear edges of terraces into which this channel belt are cut, we use this as the edge of the channel. At larger drainage areas, this often represents a channel width that is significantly wider than the visible channel occupied by water in a single given satellite image.

The choice to map channels in this manner is in part based on field observations where these gravel areas are routinely inundated during higher flow events or after individual rain storms along with the variability in channel width and position (i.e. the width of the area occupied by water) observed in different satellite images taken over different years which are available within Google Earth. This means that some portion of the channel width measurements are biased towards widths largely relevant for discharges higher than the mean. In other areas, only the channel occupied by water is visible within the imagery, usually due to tree cover, so in these cases, we mapped this as the channel width. Together, our channel width measures are likely a mixture of widths relevant for mean discharges and those for higher, moderate flood discharges depending on local conditions and available imagery.

Using this methodology, we were able to measure channel widths for 26 of the 34 erosion rate basins. For the other 8 basins, the imagery available was insufficient to measure channel widths largely because the channels were completely obscured by tree cover. The results of these channel width measurements as a function of drainage area are presented in Figure S10. The underlying data for this plot and plotting algorithm are also provided in the GitHub repository.

We use the width estimates to evaluate the choice of  $k_w = 15$  and  $\omega_a = 0.5$ , specifically by combining equation S3 and S9 to derive a relationship between width, runoff, and drainage area,

$$w = k_w R^{\omega_a} A^{\omega_a c} \quad (\text{S10})$$

We again assume  $c = 1$  and use the discharge data for the gauged basins to calculate runoffs,  $R$ , at the mean discharge and a moderate flood, i.e. the discharge associated with the 2-year flood. We then evaluate this relationship at a series of reference drainage areas that span the areas within our measured width data. Comparisons between the predicted width-drainage area relationship and those measured suggest reasonable agreement, and thus that the choice of  $k_w$  and  $\omega_a$  appear appropriate (Figure S10). At a given drainage area, the predicted widths also span much of the range of measured widths and further highlight that our measurements likely reflect a mixture of widths reflective of mean discharges and higher, moderate flood discharges. It is also worth highlighting that the lack of a clear relationship between channel width and mean basin erosion rate suggests that adjustment of channel width as opposed to slope is not a robust explanation for the  $k_{\text{sn}}\text{-E}$  pattern in the Greater Caucasus. This analysis does assume there is no specific difference in the relations between width, drainage area, runoff, and discharge within the gauged basins compared (which we use to calculate the width for the mean and 2 year flood event) and the erosion rate basins (which we used to measure the widths). Given that we are already assuming some amount of correspondence between behavior in the gauged basins and erosion rate basins to estimate mean runoff and variability, we consider this appropriate.

This finally leaves estimation of  $k_e$  and  $\tau_c$ , which together dictate the threshold term  $\Psi_c$ :

$$\Psi_c = k_e \tau_c^a \quad (\text{S11})$$

$\tau_c$  can be estimated from the grain size distribution within channels [e.g., DiBiase and Whipple, 2011], but we presently do not have (and are not aware of any published) estimates of grain size distributions for streams in the Greater Caucasus. In the absence of such grain size data, we first use a fixed  $\tau_c$  of 45 Pa. Relating this back to grain size and using a Shields criterion with a critical Shields stress of 0.3 and densities for sediment ( $\rho_s$ ) and water ( $\rho_w$ ) densities of 2700 and 1000 kg\*m<sup>-3</sup> respectively [after DiBiase and Whipple, 2011],

$$\tau_c = 0.3(\rho_s - \rho_w)D_{50} \quad (\text{S12})$$

a  $\tau_c$  of 45 Pa corresponds to a  $D_{50}$  of 90 mm. We consider this a reasonable approximation as this lies between the median (79 mm) and mean (107 mm) of the large compilation of  $D_{50}$  values from a variety of different types of steep mountain streams [e.g. Palucis and Lamb, 2017].

Fixing  $\tau_c$  to 45 Pa, we then estimate acceptable ranges of  $k_e$  values. To do this, we first wish to define a single set of shape and scale parameters for each cluster. We implement this in two ways, one via simply taking the mean of the shape and scale parameters within the clusters, but since the shape and scale parameters are linked, we wished to also try to assess whether this simple mean approach was valid (i.e., did it sever the link between shape and scale). To assess this, we produced an aggregate distribution of discharge for each basin by binning exceedance frequency space and calculating mean  $Q^*$  values within each bin. We then refit this aggregate distribution via the previously described methods. Ultimately, the shape and scale parameters estimated in this way were not particularly different than simple means, but we use these aggregate values in subsequent analyses.

Now with a single shape and scale parameter for each of the four clusters, we set about finding acceptable  $k_e$  values. To do this, for each erosion rate basin, we took the observed  $k_{sn}$  and  $^{10}\text{Be}$  erosion rate and used their uncertainties to generate a synthetic sample of 500 random E and  $k_{sn}$  pairs. For each random  $k_{sn}$ , we find a best fit  $k_e$  by using the estimated  $R$  for that basin and the aggregate shape and scale parameter for the appropriate cluster within STIM to minimize the square of the difference between a randomly selected E and the predicted E. We do this for the entire random population of  $k_{sn}$  generating a population of  $k_e$  for each basin. From this population, we select the median (because the distributions of  $k_e$  is skewed) and use the interquartile range as estimate of the variability in estimated  $k_e$ . After performing this for each  $^{10}\text{Be}$  basin, we find the median of the best  $k_e$  both within clusters and for the entire population. We use the median  $k_e$  from the whole population in the subsequent analysis of the implications of STIM (e.g., Figure 9). The algorithm to perform this optimization is provided in the GitHub repository as *cluster\_and\_optimize.py*.

### 3 Supplemental Table Captions

Tables are provided as excel files as supplementary documents. The data in these tables are reproduced as text files (though spread across a wider number of files) in the GitHub repository. Below we provide captions for the supplementary tables referenced in the main text and this document.

#### 3.1 Table S1

Summary of topographic, rainfall, and discharge statistics for gauged basins from the Global Runoff Data Centre (GRDC).

#### 3.2 Table S2

Location of all samples collected in the Caucasus region and the result of these samples (either Data, indicating that we report a  $^{10}\text{Be}$  erosion rate for this basin, Failed with reason for failure specified, or Not Analyzed).

#### 3.3 Table S3

Master table reporting data for the basins for which we report  $^{10}\text{Be}$  erosion rates. This excel table has multiple sheets, including Topography, Climate, Lithology, Quartz Masses, Be Measurements, Be Blanks, CRONUS v3 Inputs, Main Erosion Rates, CROSNSU v3 Litho Inputs, Litho Erosion Rates, CRONUS v3 Low Z Inputs, Low Z Erosion Rates, CRONUS v3 High Z Inputs, High Z Erosion Rates. The first sheet contains a readme with descriptions of each sheet.

## 4 Supplemental Figures and Captions

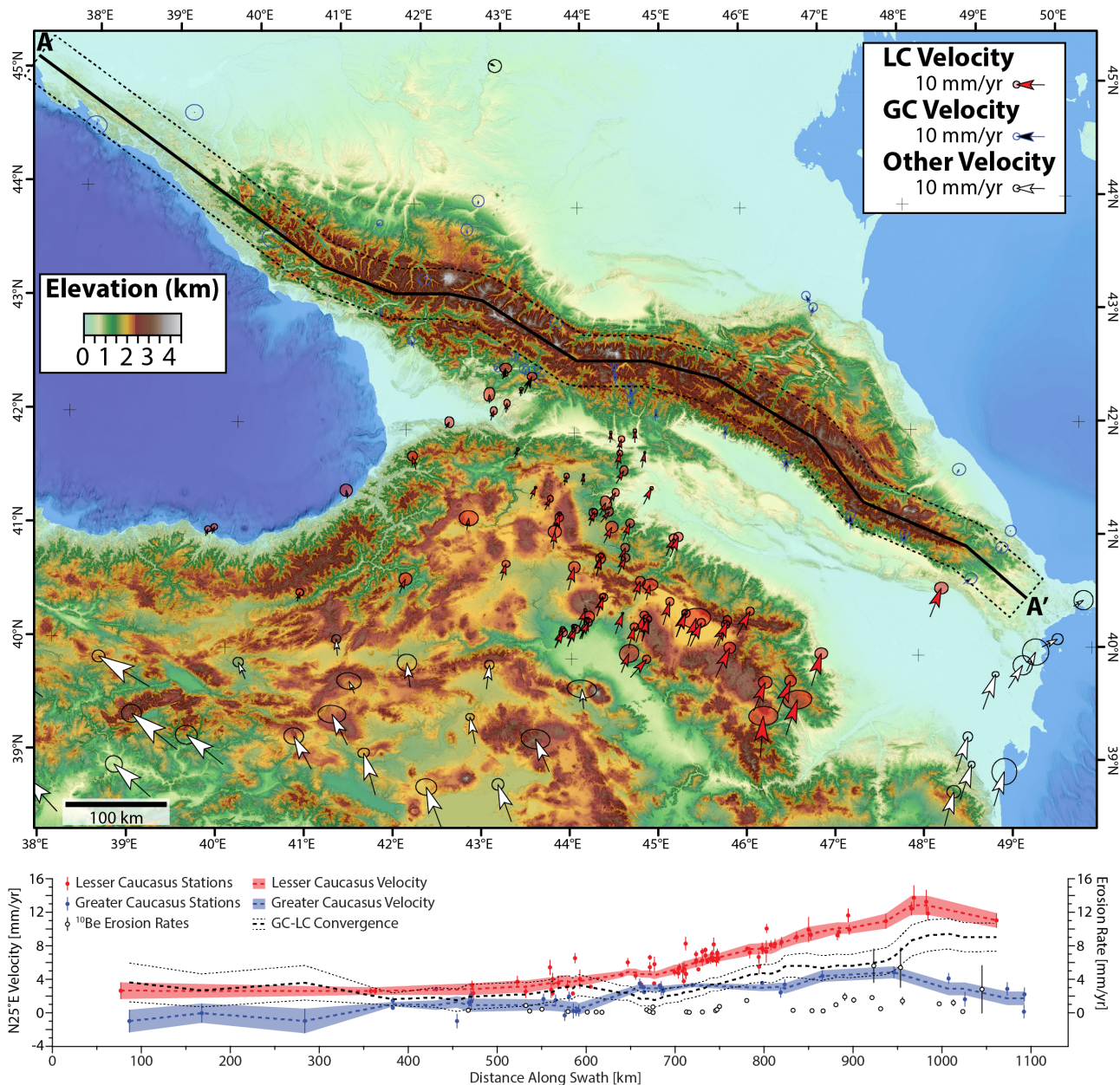


Figure S1: GPS stations within the Greater Caucasus regions from Reilinger et al. [2006], Kadirov et al. [2012], Sokhadze et al. [2018]. GPS swath is the same as in Figure 1.

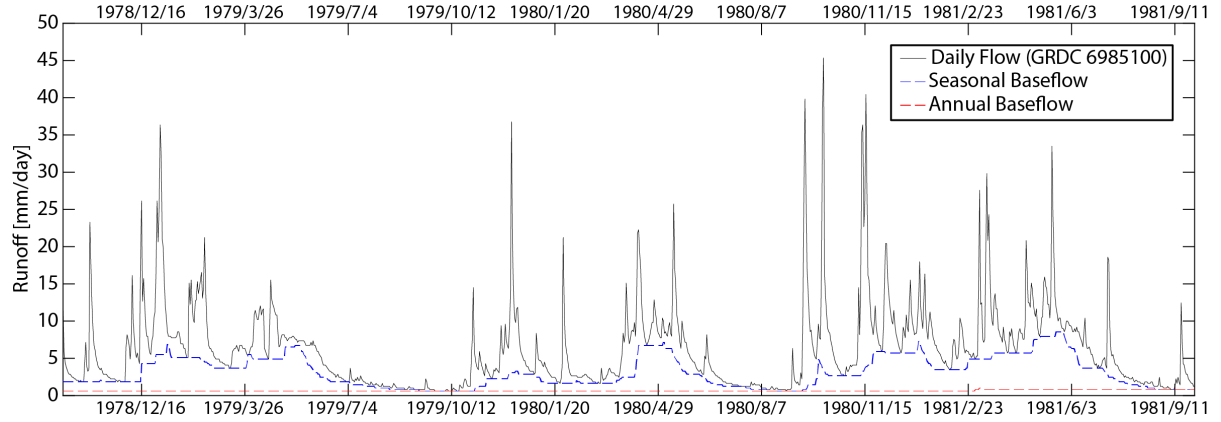


Figure S2: Example event , seasonal , and annual component separation.

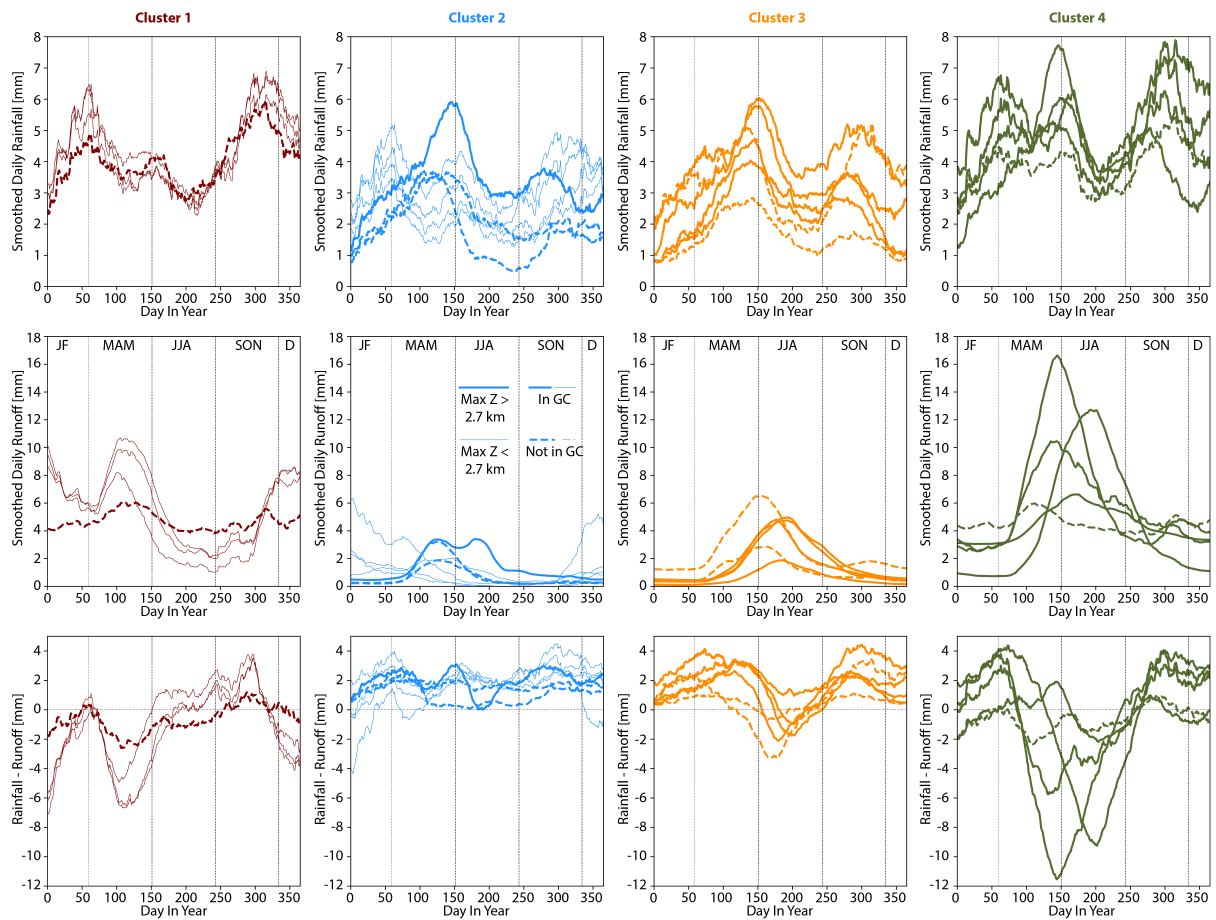


Figure S3: Upper: Averaged and smoothed rainfall time series, Middle: Averaged and smoothed runoff time series, and Bottom: Rainfall-Runoff. Watersheds are broken up by cluster from k-means clustering analysis from Figure 5 in main text. Meaningful differences in patterns were found if the data was filtered between watersheds with a maximum elevation greater or less than 2.7 km

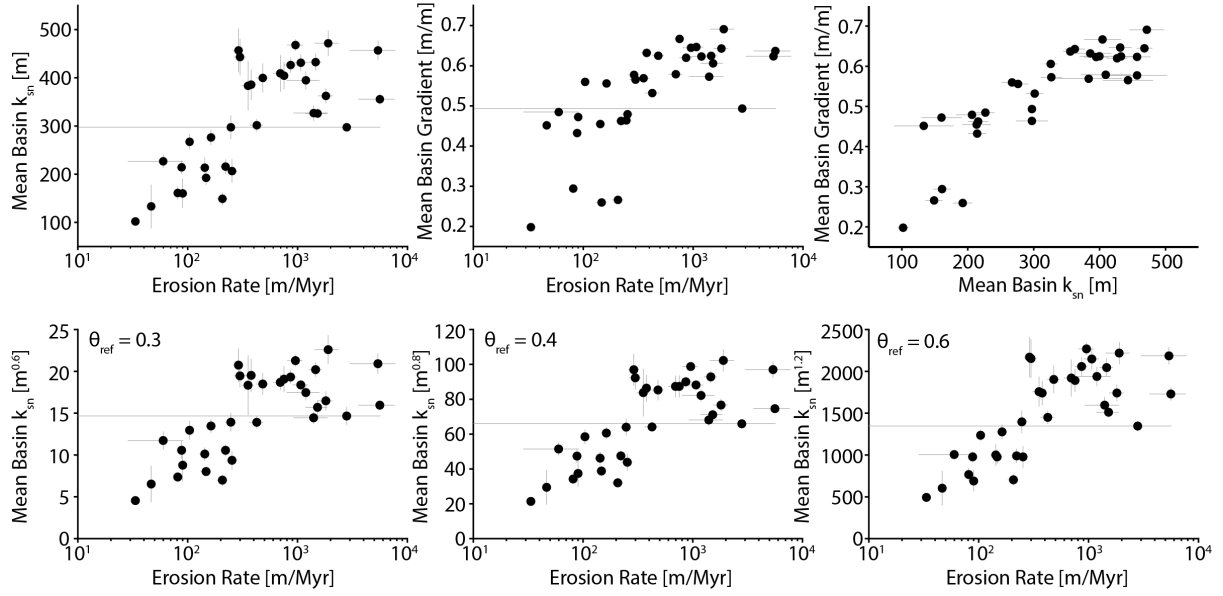


Figure S4: Top row shows basic relationships between  $k_{sn}$ , gradient and  $^{10}\text{Be}$  erosion rates. Bottom row shows  $k_{sn}$  -  $^{10}\text{Be}$  relationships with  $k_{sn}$  calculated at different  $\theta_{ref}$  values.

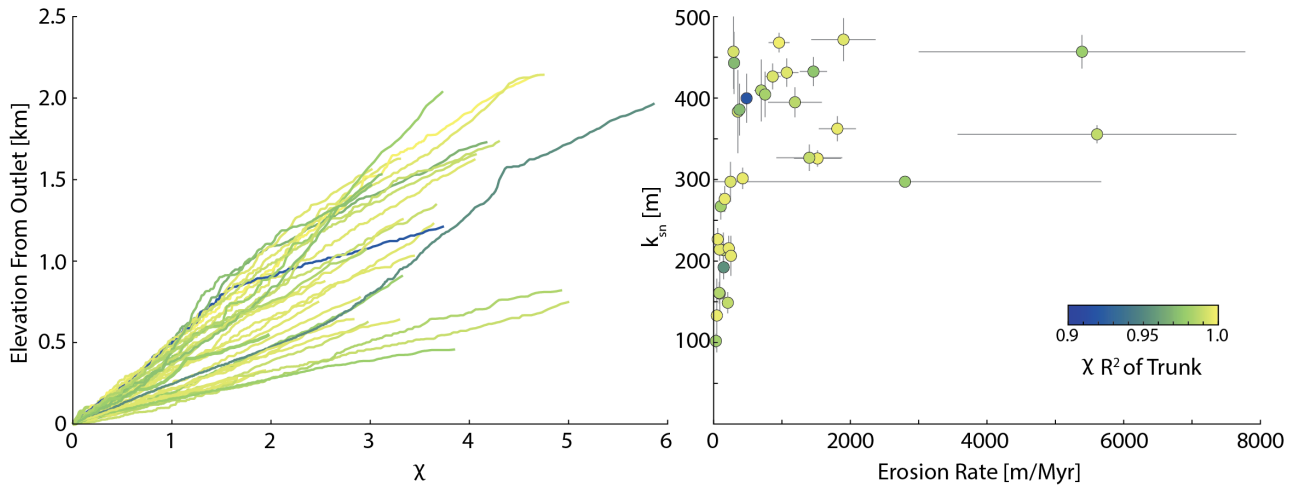


Figure S5:  $\chi$  - elevation plots of the trunk streams of individual basins colored by the  $\chi R^2$  of the trunk stream, and  $k_{sn}$  vs erosion rate colored by the  $\chi R^2$  of the trunk stream.

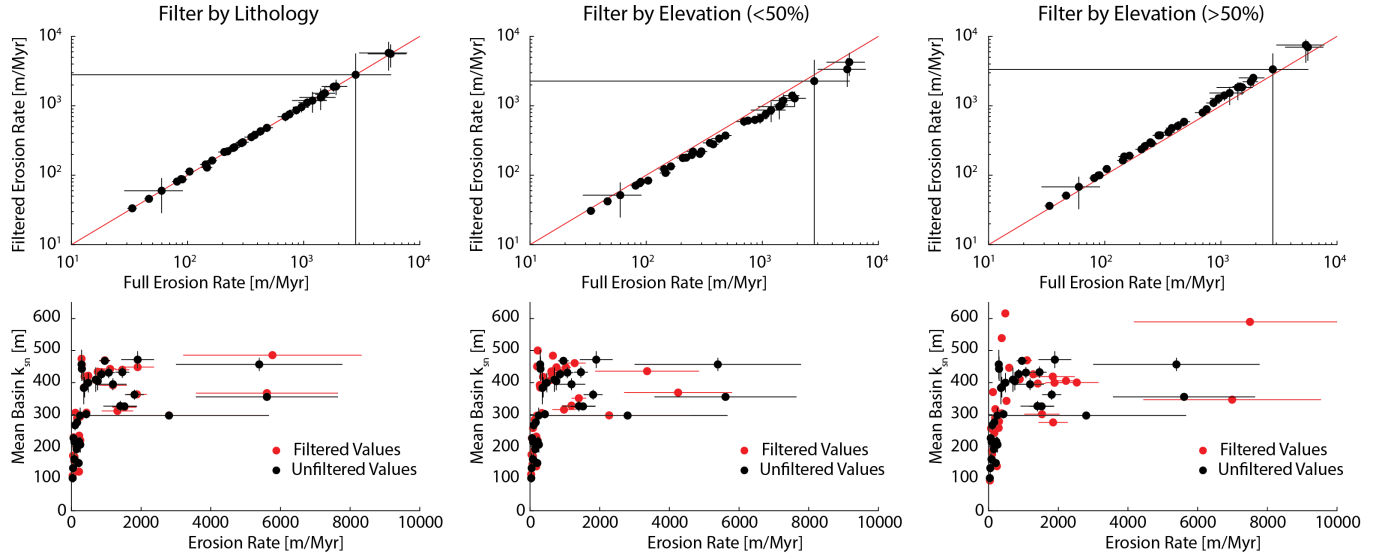


Figure S6: Comparison between erosion rates and mean basin  $k_{sn}$  as used in the main text and three different strategies for assessing the sensitivity to quartz sourcing.

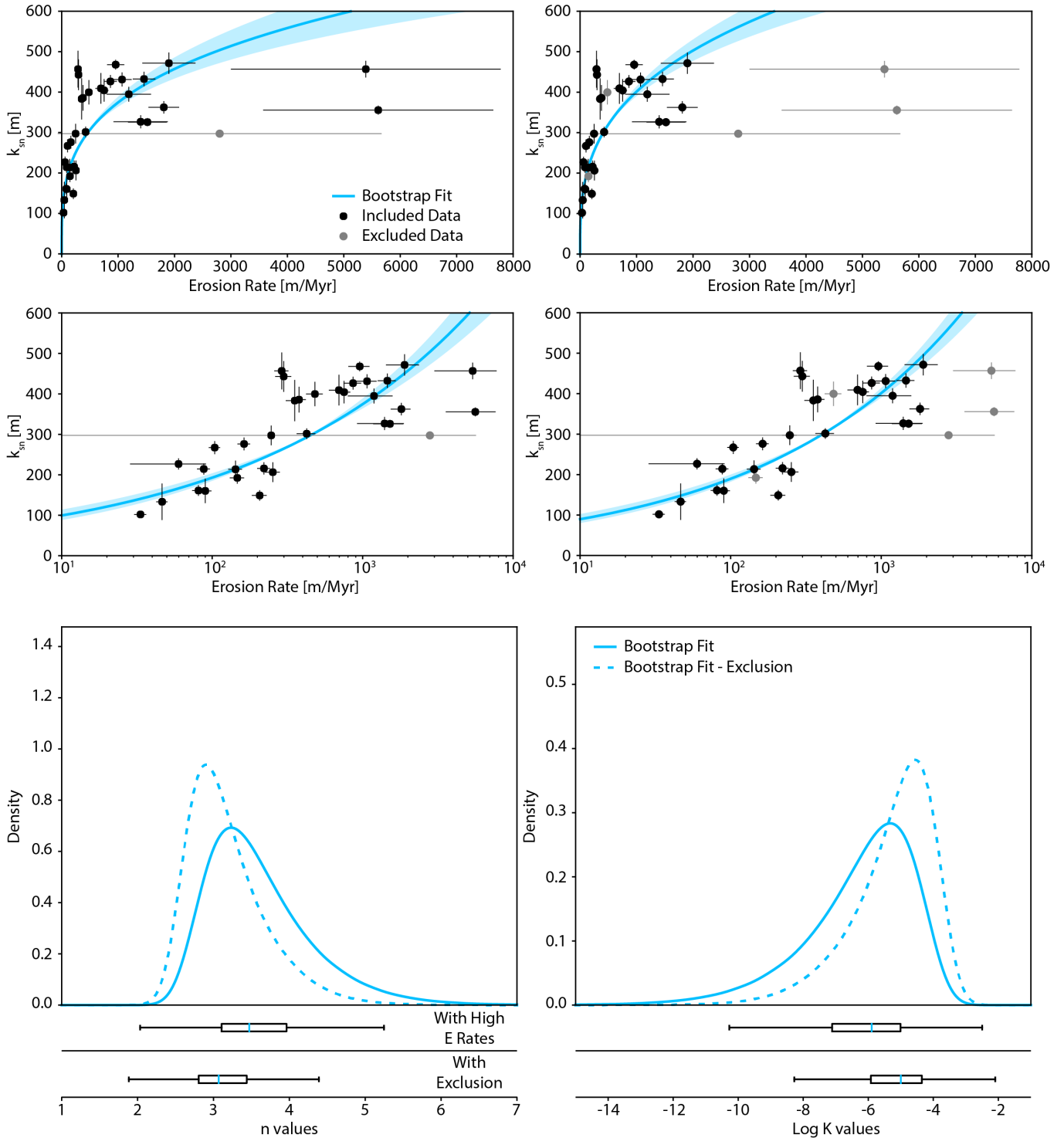


Figure S7: Power law fits to the data using a log-transformed version of the relationship and the bootstrap fitting method. Fits excluding the two highest erosion rate basins are also included. Box and whisker plots show median value with the colored line (which is used for the solid line relationship in plots above) and extent boxes represent the 25th and 75th percentiles (which are used to define the shaded regions in plots above).

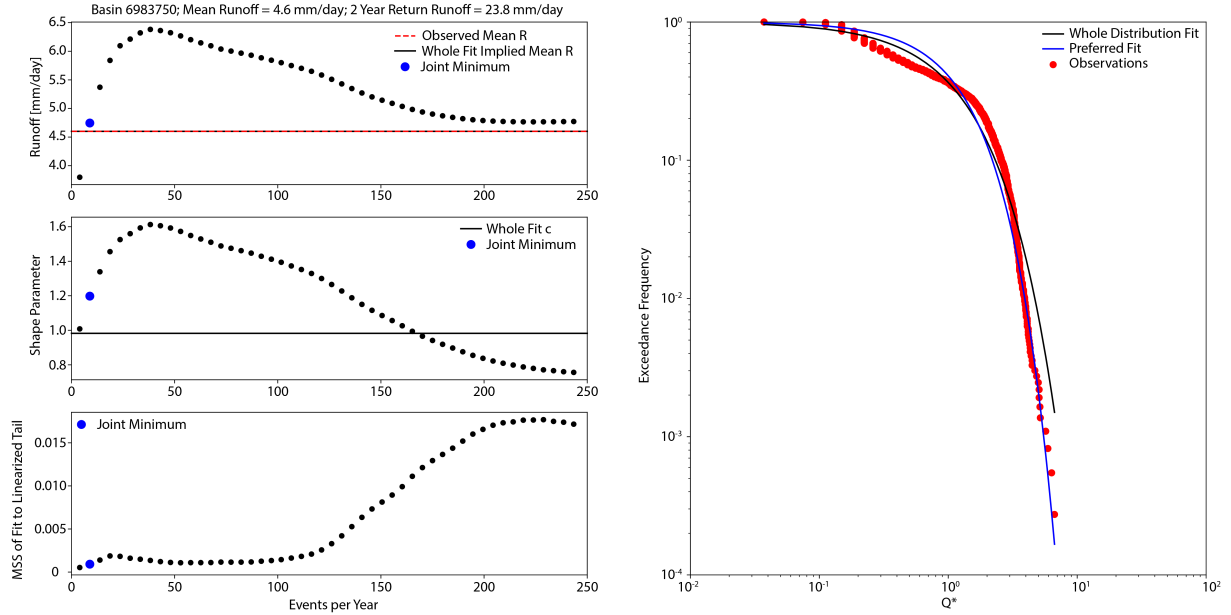


Figure S8: Representative example of the distribution fitting procedure we adopt, which attempts to minimize the joint misfit between the shape of the tail and difference between the implied and observed mean runoff.

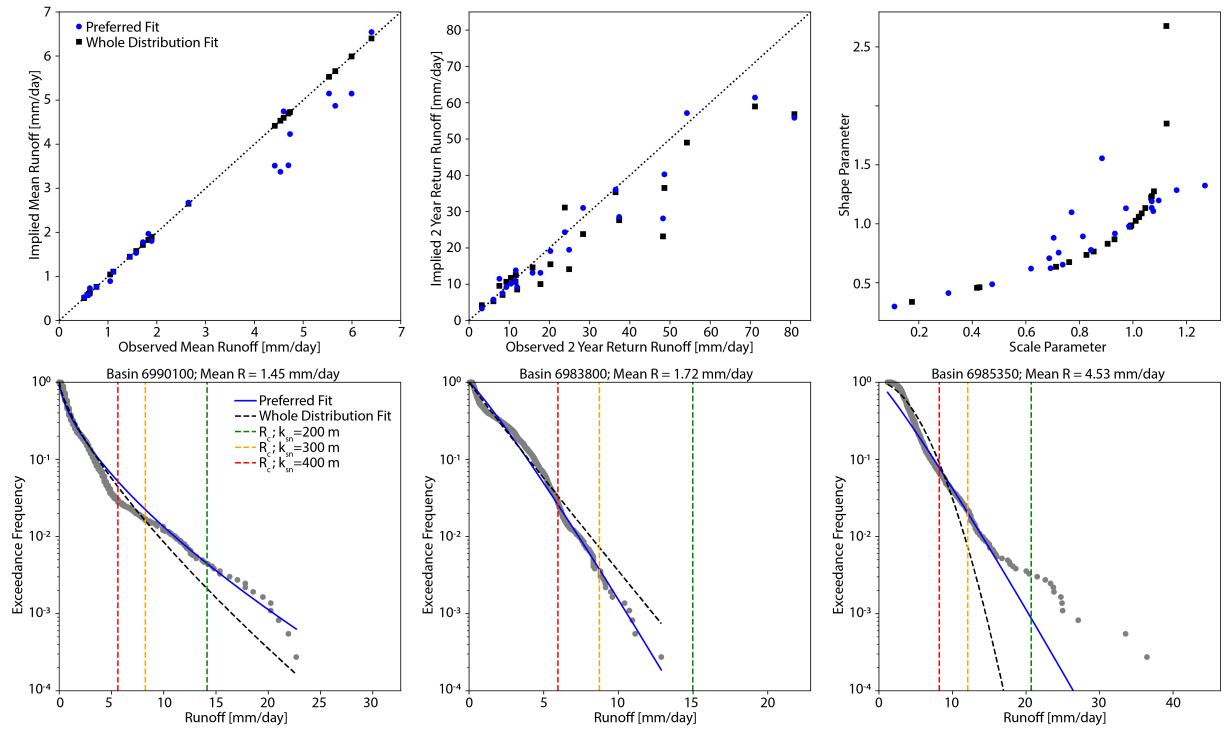


Figure S9: Top Left: Comparison of observed  $\bar{R}$  with implied  $\bar{R}$  for the preferred fitting method and a whole distribution fit using the method of moments. Top Middle: Comparison of observed and implied 2 year return runoff for the two fitting methods. Top Right: Comparison of the shape and scale parameters resultant from the two fitting methods. Bottom Panel: Implications for the two fitting methods for three representative gauged basins. Vertical lines show critical runoff (assuming the median  $k_e$  value used in the main text) for three different  $k_{sn}$  values to emphasize the importance of attempting to fit the tail of the runoff distribution correctly.

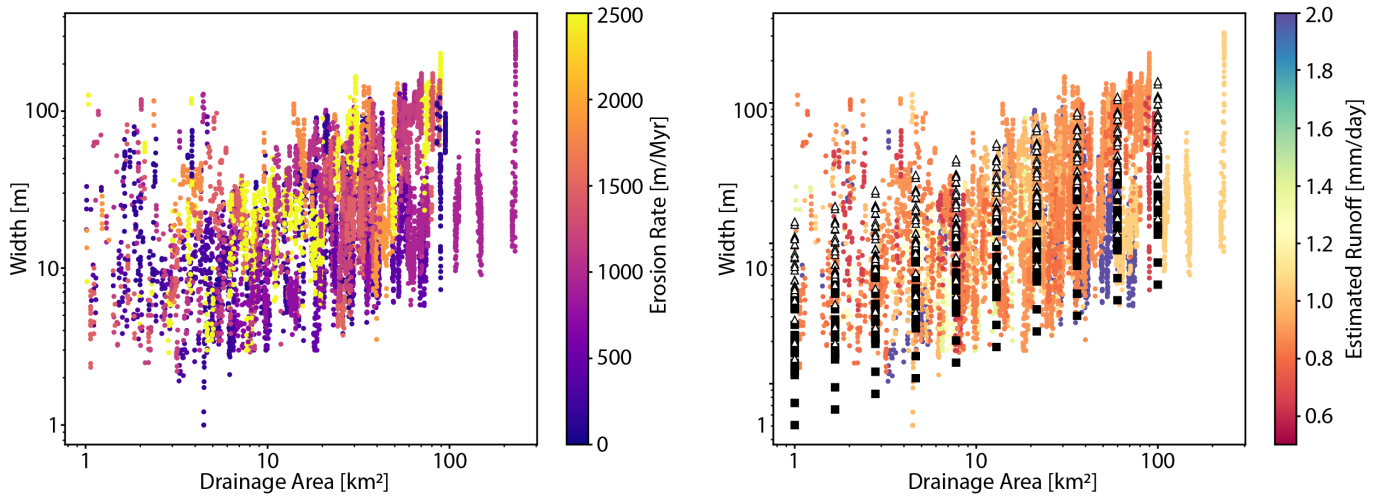


Figure S10: Comparison between widths measured on remotely sensed data and implied widths based on the choice of  $\omega_a$  and  $k_w$ .

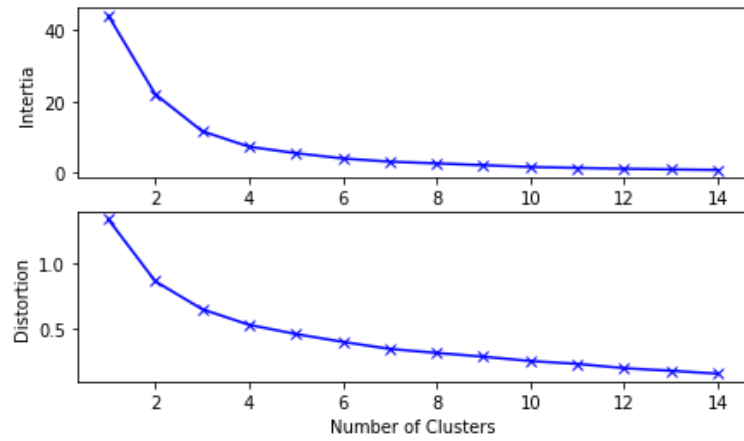


Figure S11: Elbow plot for determining ideal number of clusters in k-means clustering of variability (shape parameter) and mean runoff. Both inertia and distortion are somewhat ambiguous, but there is a potential elbow at 4 in inertia (i.e., for 5 and more clusters, the relationship between number of clusters and inertia is quasi-linear), thus we use 4 as the number of clusters.

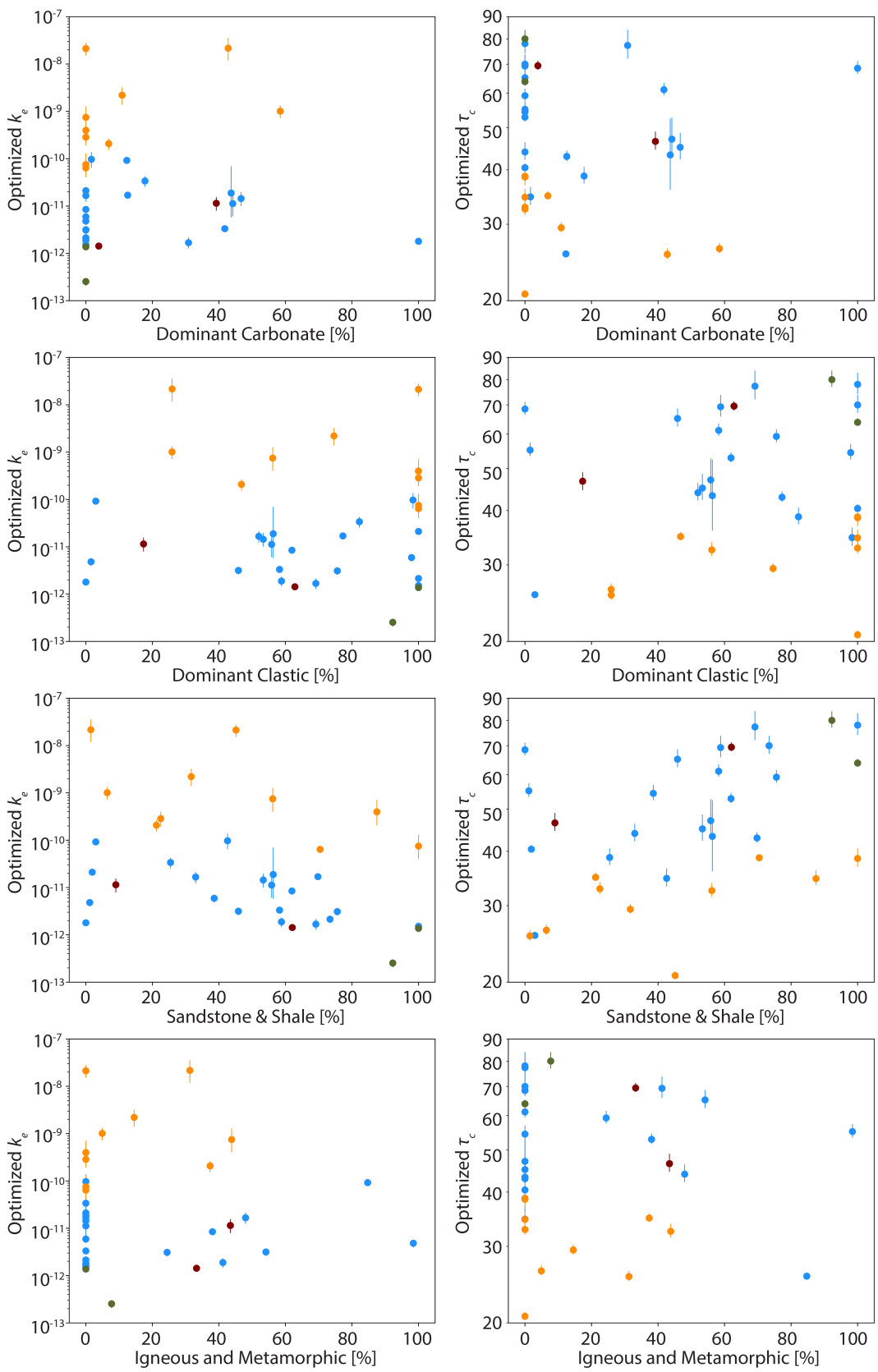


Figure S12: Variation of optimized  $k_e$ ,  $\tau_c$  and dominant lithology, colored by cluster.

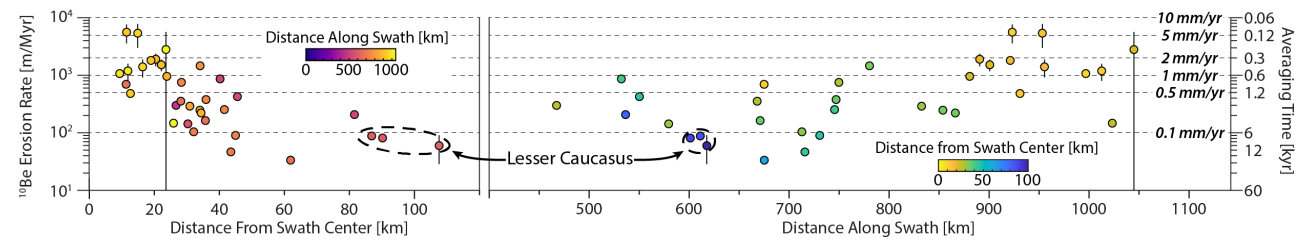


Figure S13: Erosion rate basins and their position along the swath (right) and from the center line of the swath (left), which approximates the topographic crest of the range.

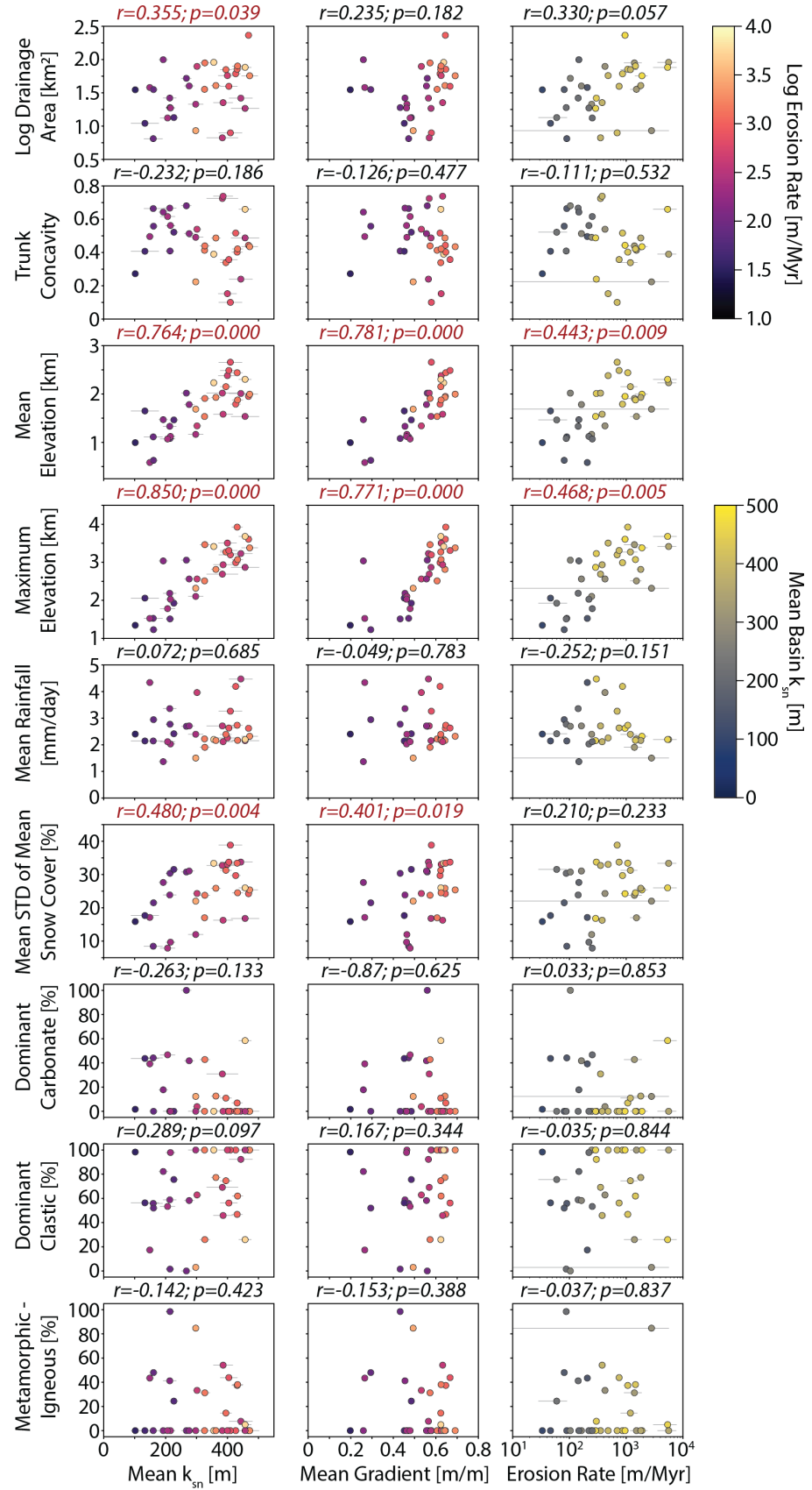


Figure S14: Comparisons of mean basin  $k_{sn}$  (left column), gradient (center column), and  $^{10}\text{Be}$  (right column) against various other values. Pearson's correlation coefficient and significance (p-value) are shown for each relationship, those colored in red indicate a p value suggesting the relationship between the the two variable is significant at the 95% confidence level.

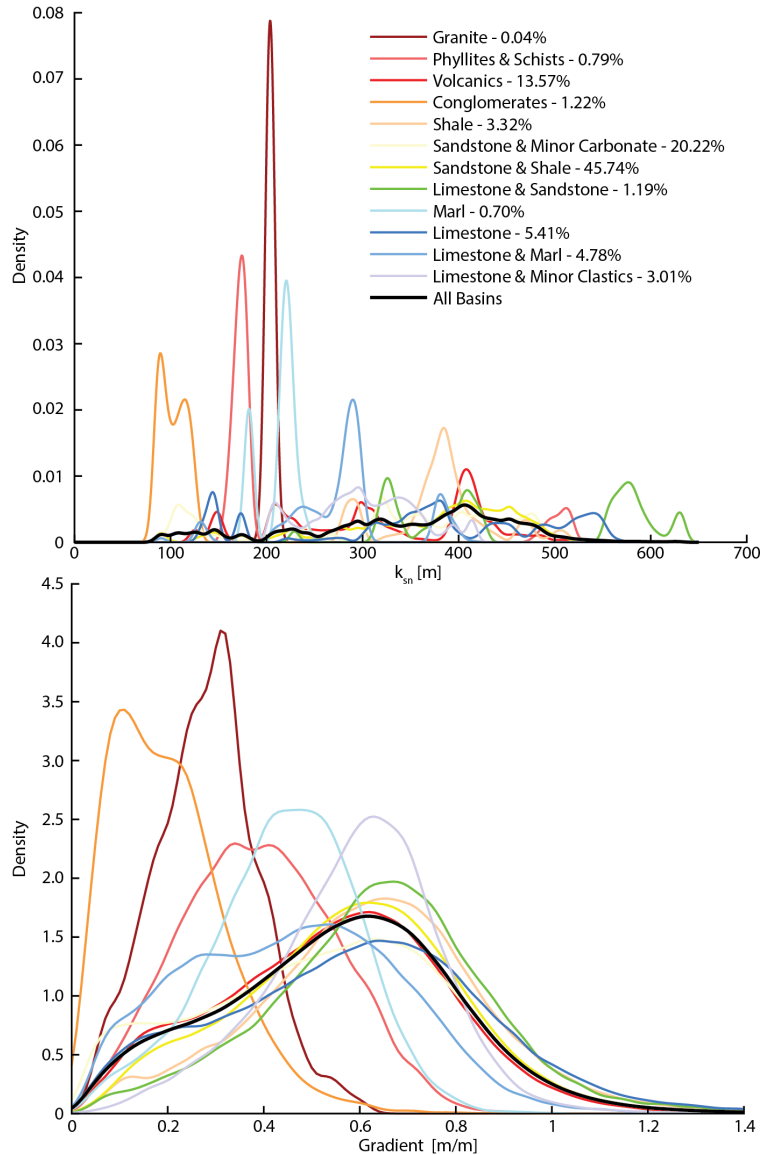


Figure S15: Kernel density estimates of  $k_{sn}$  (top) and gradient within specific lithologies. Percentages within explanation represent the fraction of the area within the entire population of sampled watersheds occupied by that lithology.

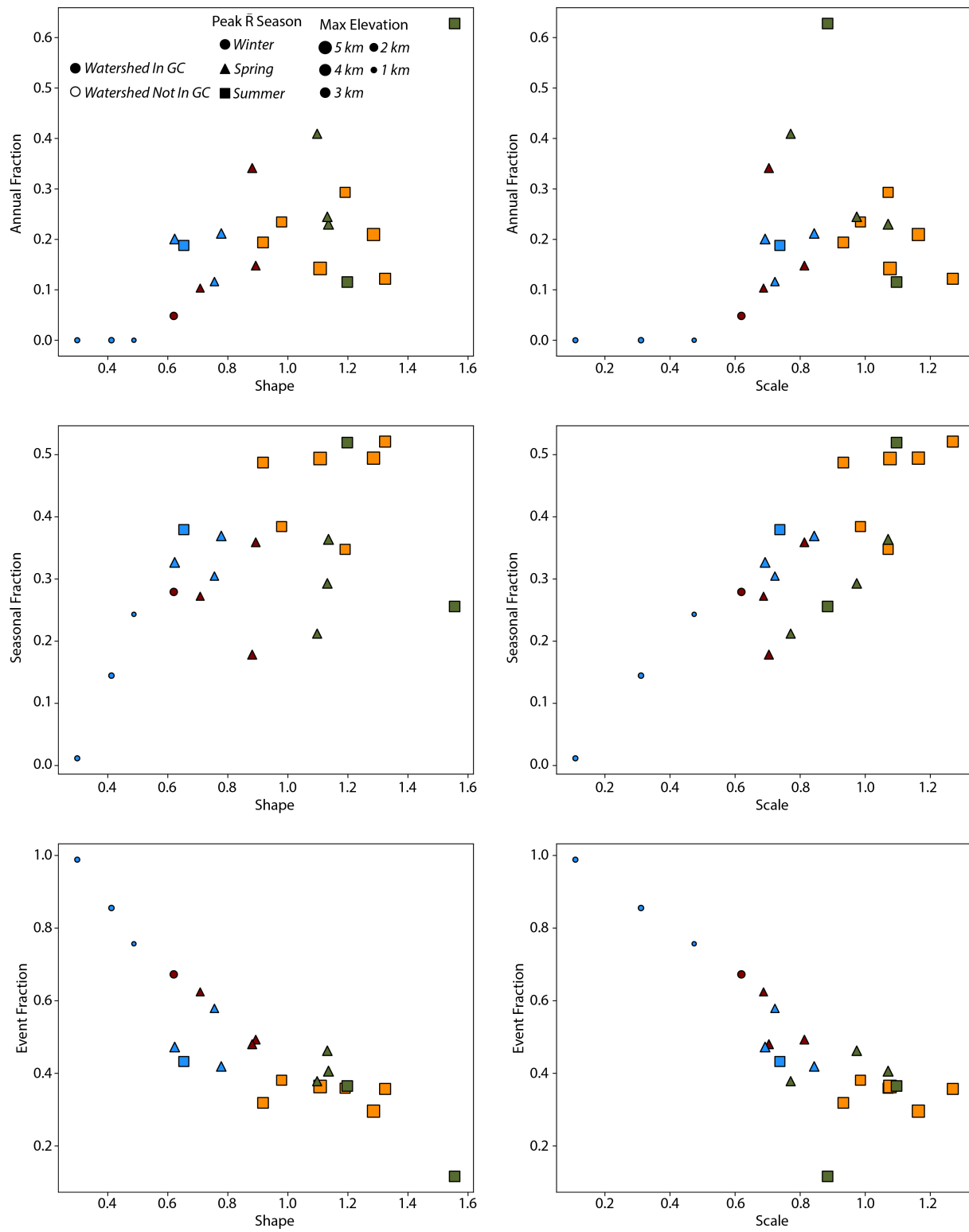


Figure S16: Comparisons of Annual Fraction (top row), Seasonal Fraction (middle row), and Event Fraction (bottom row) with the shape (left column) and scale (right column) parameters.

## References

- Byron A. Adams, Kelin X. Whipple, Adam M Forte, Arjun M. Heimsath, and Kip V. Hodges. Climate controls on erosion in tectonically active landscapes. *Science Advances*, 6(42), 2020. doi: 10.1126/sciadv.aaz3166.
- Greg Balco, J Stone, N A Lifton, and Tibor Dunai. A complete and easily accessible means of calculating surface exposure ages or erosion rates from  $^{10}\text{Be}$  and  $^{26}\text{Al}$  measurements. *Quaternary Geochronology*, 3:174–195, 2008. doi: 10.1016/j.quageo.2007.12.001.
- Roman A. DiBiase. Short Communication: Increasing vertical attenuation length of cosmogenic nuclide production on steep slopes negates topographic shielding corrections for catchment erosion rates. preprint, Cross-cutting themes: Geochronology applied to establish timing and rates of Earth surface processes, July 2018. URL <https://esurf.copernicus.org/preprints/esurf-2018-48/esurf-2018-48.pdf>.
- Roman A DiBiase and Kelin X Whipple. The influence of erosion thresholds and runoff variability on the relationships among topography, climate, and erosion rate. *Journal of Geophysical Research*, 116(F04036), 2011. doi: 10.1029/2011JF002095.
- R.G. Ditchburn and N.E. Whitehead. The separation of  $^{10}\text{Be}$  from silicates. In *3rd Workshop of the South Pacific Environmental Radioactivity Association*, pages 4–7, 1994.
- G. Burch Fisher, Bodo Bookhagen, and Colin B. Amos. Channel planform geometry and slopes from freely available high-spatial resolution imagery and DEM fusion: Implications for channel width scalings, erosion proxies, and fluvial signatures in tectonically active landscapes. *Geomorphology*, 194:46–56, 2013. ISSN 0169-555X. doi: 10.1016/j.geomorph.2013.04.011. URL <http://dx.doi.org/10.1016/j.geomorph.2013.04.011>.
- Adam M Forte and Kelin X Whipple. Short communication : The Topographic Analysis Kit (TAK) for TopoToolbox. *Earth Surface Dynamics*, 7:87–95, 2019. doi: 10.5194/esurf-7-87-2019.
- Adam M Forte, Eric Cowgill, and Kelin X Whipple. Transition from a singly vergent to doubly vergent wedge in a young orogen: The Greater Caucasus. *Tectonics*, 33(11):2077–2101, 2014. doi: 10.1002/2014TC003651.
- Adam M Forte, Kelin X Whipple, B Bookhagen, and Matthew W Rossi. Decoupling of modern shortening rates, climate, and topography in the Caucasus. *Earth and Planetary Science Letters*, 449:282–294, 2016. doi: 10.1016/j.epsl.2016.06.013.
- Ramin Gobejishvili, Nino Lomidze, Levan Tielidze, and Jaap J M van der Meer. Late Pleistocene (Würmian) Glaciations of the Caucasus. In J Ehlers, P L Gibbard, and P D Hughes, editors, *Quaternary glaciations - Extent and chronology*, pages 141–147. Elsevier, Amsterdam, 2011.
- Fakhraddin Kadirov, Michael Floyd, Akif Alizadeh, Ibrahim Guliev, R Reilinger, Sadi Kuleli, R King, and M N Toksoz. Kinematics of the eastern Caucasus near Baku, Azerbaijan. *Natural Hazards*, 63:997–1006, 2012.
- A. M. G. Klein Tank, J. B. Wijngaard, G. P. Können, R. Böhm, G. Demarée, A. Gocheva, M. Mileta, S. Pashiardis, L. Hejkrlik, C. Kern-Hansen, R. Heino, P. Bessemoulin, G. Müller-Westermeier, M. Tzanakou, S. Szalai, T. Pálsdóttir, D. Fitzgerald, S. Rubin, M. Capaldo, M. Maugeri, A. Leitass, A. Bukanis, R. Aberfeld, A. F. V. van Engelen, E. Forland, M. Mietus, F. Coelho, C. Mares, V. Razuvaev, E. Nieplova, T. Cegnar, J. Antonio López, B. Dahlström, A. Moberg, W. Kirchhofer, A. Ceylan, O. Pachaliuk, L. V. Alexander, and P. Petrovic. Daily dataset of 20th-century surface air temperature and precipitation series for the European Climate Assessment: EUROPEAN TEMPERATURE AND PRECIPITATION SERIES. *International Journal of Climatology*, 22(12):1441–1453, October 2002. ISSN 08998418. doi: 10.1002/joc.773. URL <http://doi.wiley.com/10.1002/joc.773>.
- C. Kohl and K. Nishizumi. Chemical isolation of quartz for measurement of in situ-produced cosmogenic nuclides. *Geochimica et Cosmochimica Acta*, 56(9):3583–3587, 1992.
- Dimitri Lague, N Hovius, and P Davy. Discharge, discharge variability, and the bedrock channel profile. *Journal of Geophysical Research*, 110:F04006–F04006, 2005. doi: 10.1029/2004JF000259.
- Charles Mifsud, Toshiyuki Fujioka, and David Fink. Extraction and purification of quartz in rock using hot phosphoric acid for in situ cosmogenic exposure dating. *Nuclear Instruments and Methods in Physics Research B*, 294:203–207, 2013. ISSN 0168-583X. doi: 10.1016/j.nimb.2012.08.037. URL <http://dx.doi.org/10.1016/j.nimb.2012.08.037>.
- Nathan A Niemi, Michael Oskin, Douglas Burbank, Arjun M Heimsath, and Emmanuel J Gabet. Effects of bedrock landslides on cosmogenically determined erosion rates. *Earth and Planetary Science Letters*, 237:480–498, 2005.

M. C. Palucis and M. P. Lamb. What controls channel form in steep mountain streams?: Controls on Steep Channel Form. *Geophysical Research Letters*, 44(14):7245–7255, July 2017. ISSN 00948276. doi: 10.1002/2017GL074198. URL <http://doi.wiley.com/10.1002/2017GL074198>.

Eric W Portenga and Paul R Bierman. Understanding Earth's eroding surface with  $^{10}\text{Be}$ . *GSA Today*, 21(8):4–10, 2011. doi: 10.1130/G111A.1.

R Reilinger, S McClusky, Philippe Vernant, S Lawrence, S Ergintav, Rahsan Cakmak, Haluk Ozener, Fakhreddin Kadirov, Ibrahim Guliev, Ruben Stepanyan, M Nadariya, Galaktion Hahubia, S Mahmoud, K Sakr, Abdullah ArRajehi, D Paradissis, A Al-Aydrus, M Prilepin, Tamara Guseva, Emre Evren, Andriy Dmitrotsa, S V Filikov, Francisco Gomez, Riad Al-Ghazzi, and Gebran Karam. GPS constraints on continental deformation in the Africa-Arabia-Eurasia continental collision zone and implications for the dynamics of plate interactions. *Journal of Geophysical Research*, 111:doi:10.1029/2005JB004051–doi:10.1029/2005JB004051, 2006.

Matthew W Rossi, Kelin X Whipple, and Enrique R Vivoni. Precipitation and evapotranspiration controls on event-scale runoff variability in the contiguous United States and Puerto Rico. *Journal of Geophysical Research*, 121, 2016. doi: 10.1002/2015JF003446.

W Schwanghart and D Scherler. Short Communication: TopoToolbox 2 - MATLAB based software for topographic analysis and modeling in Earth surface sciences. *Earth Surface Dynamics*, 2:1–7, 2014. doi: 10.5194/esurf-2-1-2014.

G. Sokhadze, M. Floyd, T. Godoladze, R. King, E. S. Cowgill, Z. Javakhishvili, G. Hahubia, and R. Reilinger. Active convergence between the Lesser and Greater Caucasus in Georgia: Constraints on the tectonic evolution of the Lesser–Greater Caucasus continental collision. *Earth and Planetary Science Letters*, 481:154–161, 2018. doi: 10.1016/j.epsl.2017.10.007. URL <https://www.sciencedirect.com/science/article/pii/S0012821X17305666>.

John O. Stone. Air pressure and cosmogenic isotope production. *Journal of Geophysical Research: Solid Earth*, 105(B10): 23753–23759, October 2000. ISSN 01480227. doi: 10.1029/2000JB900181. URL <http://doi.wiley.com/10.1029/2000JB900181>.

J. V. Sutcliffe, F. A. K. Farquharson, E. L. Tate, and S. S. Folwell. Flood regimes in the Southern Caucasus: the influence of precipitation on mean annual floods and frequency curves. *Hydrology Research*, 39(5-6):385–401, October 2008. ISSN 0029-1277, 2224-7955. doi: 10.2166/nh.2008.025. URL <https://iwaponline.com/hr/article/39/5-6/385/906/Flood-regimes-in-the-Southern-Caucasus-the>.

Gregory E Tucker. Drainage basin sensitivity to tectonic and climatic forcing: Implications of a stochastic model for the role of entrainment and erosion thresholds. *Earth Surface Processes and Landforms*, 29:185–204, 2004. doi: 10.1002/esp.1020.

P. S. Wilson and R. Toumi. A fundamental probability distribution for heavy rainfall: DISTRIBUTION FOR HEAVY RAINFALL. *Geophysical Research Letters*, 32(14):n/a–n/a, July 2005. ISSN 00948276. doi: 10.1029/2005GL022465. URL <http://doi.wiley.com/10.1029/2005GL022465>.

H Wulf, B Bookhagen, and D Scherler. Differentiating between rain, snow, and glacier contributions to river discharge in the western Himalaya using remote-sensing data and distributed hydrologic modeling. *Advances in Water Resources*, 88: 152–169, 2016. doi: 10.1016/j.advwatres.2015.12.004.

B J Yanites, Gregory E Tucker, and Robert S Anderson. Numerical and analytical models of cosmogenic radionuclide dynamics in landslide-dominated drainage basins. *Journal of Geophysical Research*, 114:F01007–F01007, 2009. doi: 10.1029/2008JF001088.

Brian J. Yanites, Nate A. Mitchell, Joshua C. Bregy, Grace A. Carlson, Kirstyn Cataldo, Margaret Holahan, Graham H. Johnston, Amelia Nelson, Jeffery Valenza, and Matthew Wanker. Landslides control the spatial and temporal variation of channel width in southern Taiwan: Implications for landscape evolution and cascading hazards in steep, tectonically active landscapes: Variation in channel morphology controlled by landslides in s. Taiwan. *Earth Surface Processes and Landforms*, 43 (9):1782–1797, July 2018. ISSN 01979337. doi: 10.1002/esp.4353. URL <http://doi.wiley.com/10.1002/esp.4353>.